

Contribution of hydroxymethane sulfonate to ambient particulate matter: A potential explanation for high particulate sulfur during severe winter haze in Beijing

Jonathan M. Moch¹, Eleni Dovrou², Loretta J. Mickley², Frank N. Keutsch^{2,3}, Yuan Cheng⁴, Daniel J. Jacob^{1,2}, Jingkun Jiang^{5,6}, Meng Li^{7,8}, J. William Munger^{1,2}, Xiaohui Qiao^{5,6}, Qiang Zhang^{7,9}

¹ Department of Earth and Planetary Sciences, Harvard University, Cambridge, MA, USA

² John A. Paulson School of Engineering and Applied Sciences, Harvard University, Cambridge, MA, USA

³ Department of Chemistry and Chemical Biology, Harvard University, Cambridge, MA, USA

⁴ School of Environment, Harbin Institute of Technology, Harbin, China

⁵ State Key Joint Laboratory of Environmental Simulation and Pollution Control, School of Environment, Tsinghua University, Beijing, China

⁶ State Environmental Protection Key Laboratory of Sources and Control of Air Pollution Complex, Tsinghua University, Beijing, China

⁷ Ministry of Education Key Laboratory for Earth System Modeling, Department for Earth System Science, Tsinghua University, Beijing, China

⁸ Max-Planck Institute for Chemistry, Mainz, Germany

⁹ Collaborative Innovation Center for Regional Environmental Quality, Beijing, China

Contents of this file

Section S1. Proposed alternative sulfur oxidation mechanisms

Section S2. 1-D model simulations

Section S3. Comparison of cloud products, associated uncertainty, and trends

Section S4. GEOS-Chem model simulations

Section S5. Methodology followed to detect HMS using an IC system

Section S6. Sensitivity simulations

Figure S1. Timeseries of hourly liquid water path (LWP) in low clouds (> 700 hPa) in Beijing for December 2011 and January 2013

Figure S2. Example chromatographs for the detection of HMS using an Ion Chromatography system.

Figure S3. Timeseries of hourly HMS concentrations in Beijing in January 2013, calculated by an ensemble of sensitivity studies.

Figure S4. Simulated surface concentrations of HCHO from the 1-D model during January 2013.

Figure S5. Timeseries of monthly mean liquid water path (LWP) in low clouds (> 700 hPa) for the winter months

Table S1. Constants used in 1-D model

S1. Proposed alternative sulfur oxidation mechanisms

Proposed alternative mechanisms for sulfur oxidation during Beijing haze include (1) aqueous phase transition metal catalyzed oxidation of SO_2 (Alexander et al., 2009; Y.F. Cheng et al., 2016), (2) heterogeneous oxidation of SO_2 on deliquescent non-dust aerosols (Y. Wang et al., 2014), and (3) aqueous phase oxidation of SO_2 by NO_2 under high pH conditions (Y.F. Cheng et al., 2016; G. Wang et al., 2016). These mechanisms all have limited experimental evidence or are too small a sulfate source to explain observations. For example, while the heterogeneous oxidation of SO_2 on dust has been well studied (Fairlie et al., 2010; Harris et al., 2013), there is little laboratory or field evidence of such chemistry on deliquescent non-dust aerosols, which in any case would depend on sufficient levels of OH, O_3 , and H_2O_2 (Zhang and Carmichael, 1999). Transition metal catalyzed SO_2 oxidation has been shown to be inadequate to explain observations of high particulate sulfur during extreme haze (Y.F. Cheng et al., 2016). Oxidation of SO_2 by NO_2 requires aerosol pH close to neutral, but observations suggest aerosol pH levels of ~4-5 regardless of high ammonia levels (Liu et al., 2017; Guo et al., 2017; Song et al., 2018). This reaction also has the additional problem of being self-limiting, as increasing sulfate would decrease aerosol pH and therefore the reaction rate (G. Wang et al., 2016).

S2. 1-D model simulations

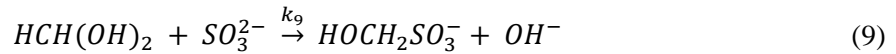
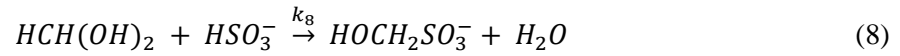
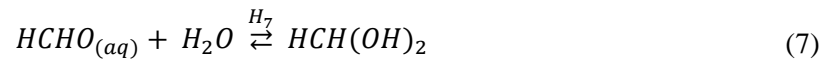
We construct a 1-D model, from the surface to ~700 m, to simulate aqueous phase chemistry in the boundary layer during two winter haze events in Beijing – December 9-29, 2011, and January 9-17, 2013. We estimate plausible ranges for the emissions of both HCHO and SO_2 by calculating the mean emissions required to maintain constant surface concentrations of HCHO and SO_2 in the model for each period. These HCHO and SO_2 concentrations are based on observations (Y. Wang et al., 2014; Rao et al., 2016).

Cloud liquid water content, vertical temperature profiles, and pressure profiles in the model are from the Modern-Era Retrospective Analysis for Research and Applications, version 2 (MERRA-2; Gelaro et al., 2017; <https://gmao.gsfc.nasa.gov/reanalysis/MERRA-2/>). We use these parameters to determine the presence of clouds, reaction rates, and Henry's law constants. We apply those values from the MERRA-2 grid box that includes Tsinghua University, where the observations of particulate sulfur used in this study were carried out. We divide the model into 4 layers following the meteorology in MERRA-2, which shows the mean boundary layer height between noon and 4pm local time. As a check, we calculate the MERRA-2 low cloud liquid water path (LCLWP) in clouds below 700 hPa and compare to values from the Cloud and the Earth's Radiant Energy System (CERES) instrument on

board the Terra and Aqua satellites (Minnis et al., 2011). We also use observations of surface relative humidity from the Chinese Meteorological Administration (<https://data.cma.cn/>). Details on the comparison of cloud products are in Section S3.

All differential equations in the 1-D model are solved using a variable order, variable time step solver of differential equations, with a maximum time step of 5 minutes. Solutions are reached using a backwards differential formula, also known as Gear's Method (Shampine and Reichelt, 1997).

In addition to the chemical reactions described in the main text, we also include the reaction of sulfite and bisulfite with methanediol ($\text{HCH}(\text{OH})_2$). However, these reactions proceed at a considerably slower rate than the formation of HMS via aqueous HCHO (Olson and Hoffman 1986; Kovacs et al., 2005) and thus have only a minimal contribution to HMS formation even though a large portion of HCHO in cloud droplets is in the methanediol form:



In conditions with adequate oxidants, a major sink of methanediol is the rapid reaction with aqueous OH radicals to form formic acid (HCOOH ; Jacob, 1986). However, since we assume low concentrations of oxidants during haze events, we neglect this and other oxidation reactions involving SO_2 and HCHO. We also neglect direct photolysis of HCHO, which during Beijing winter haze has a mean time scale of ~3 days in GEOS-Chem (Section S4).

The change in concentration of species i in terms of $\text{mol m}^{-3} \text{ s}^{-1}$ for a layer l and independent species j is given in the model by:

$$l = 1 \quad \frac{dn_{i,1}(t)}{dt} = P_{i,1}[n_{j,1}(t)] - L_{i,1}[n_{j,1}(t)] - \frac{2K_z \langle N_1 \rangle}{z_1 + z_2} \left(\frac{\frac{n_{i,1}(t)}{N_1} - \frac{n_{i,2}(t)}{N_2}}{z_2 - z_1} \right) + E \quad (10a)$$

$$\frac{dn_{i,l}(t)}{dt} = P_{i,l}[n_{j,l}(t)] - L_{i,l}[n_{j,l}(t)] - \frac{2K_z \langle N_l \rangle}{z_{l+1} - z_{l-1}} \left(\frac{n_{i,l}(t)}{N_l} - \frac{n_{i,l+1}(t)}{N_{l+1}} \right) - \frac{2K_z \langle N_{l-1} \rangle}{z_{l+1} - z_{l-1}} \left(\frac{n_{i,l}(t)}{N_l} - \frac{n_{i,l-1}(t)}{N_{l-1}} \right)$$

(10b)

$$\frac{dn_{i,4}(t)}{dt} = P_{i,4}[n_{j,4}(t)] - L_{i,4}[n_{j,4}(t)] - \frac{K_z \langle N_4 \rangle}{z_T - \frac{z_3 + z_4}{2}} \left(\frac{n_{i,4}(t)}{N_4} - \frac{n_{i,3}(t)}{N_3} \right) - \frac{V_e}{z_T - \frac{z_3 + z_4}{2}} (n_{i,4} - 0)$$

(10c)

91

92 in which n_i is the species concentration, P_{ij} and L_{ij} are chemical production and loss rates, N_i is the
 93 concentration of air (mol m^{-3}), $\langle N_l \rangle$ is the mean air density of layer l and $l+1$, K_z is the eddy diffusion
 94 coefficient, z_l is the height of the layer midpoint, z_T is the height of the top of layer 4, and V_e is the
 95 constant entrainment velocity of fresh air into the boundary layer. Here $l=1$ denotes the surface layer
 96 and $l=4$, the top of the boundary layer. E is the emissions rate at the surface. For HMS, E is always 0,
 97 while for SO_2 and HCHO , E is a value calculated as described below. In the base case, we set the eddy
 98 diffusion coefficient of $1 \times 10^5 \text{ cm}^2 \text{ s}^{-1}$ (Jacob et al., 1989); the entrainment velocity coefficient is always
 99 set to 0.5 cm s^{-1} . Table S1 lists the other constants used.

100 In the absence of clouds, HMS is assumed to exist in the particle phase, where it could exist as
 101 a salt with either NH_4^+ or dust as the counter ion. The identity of the counter ion would not change our
 102 results. For the surface layer, we neglect both dry and wet deposition of particles. We assume that the
 103 rate of dry deposition is low due to the stable boundary layer and small particle size. Observations
 104 from Beijing show the majority of particulate mass in fine particles (diameter $< 2.5 \mu\text{m}$), with an
 105 enhancement in the fraction of particulate mass in fine particles during heavy haze days (Wang et al.,
 106 2012; Sun et al., 2013). For fine particles in the Beijing area, the dry deposition time scale is ~ 1 week
 107 (Liu et al., 2016), compared to a ventilation time scale of ~ 1 -2 days. Wet deposition is also likely
 108 unimportant as observations show minimal precipitation during these time periods, and surface
 109 relative humidity is generally too low to be classified as fog at this time of year.

We follow a two-step procedure to calculate the emissions E of SO_2 and HCHO . Using the 1-D model, we first calculate the emissions at each time step required to maintain a constant, specified concentration of SO_2 or HCHO at the surface throughout the given time period, while allowing concentrations to change in the layers above. We call the resulting timeseries of implied emissions E_i , with each configuration of cloud pH and constant SO_2 and HCHO yielding a different E_i . The mean of each E_i timeseries is the constant emissions value E_c for that period. We next apply E_c to the 1-D model with initial concentrations of HMS , SO_2 , and HCHO set everywhere to 0. In this step, SO_2 and HCHO concentrations vary over time, with their mean values in layer 1 over the time interval approximating the constant values specified in the first step.

Chemical production and loss of HMS occur according to aqueous phase reactions 1-9. We assume chemical equilibrium between the gas and aqueous phases in each time step:

$$\begin{aligned}
 P_{\text{HMS},l}(t) &= L_{\text{SO}_2,l}(t) = L_{\text{HCHO},l}(t) \\
 &= \left[\left(\frac{n_{\text{SO}_2,l}(t)}{N_l} \right) P_l \right. \\
 &\quad \left. + k_5 H_1 H_2 \frac{\left(\frac{n_{\text{SO}_2,l}(t)}{N_l} \right) P_l}{10^{-(\text{cloud pH})}} \right. \\
 &\quad \left. + k_6 H_1 H_2 H_3 \frac{\left(\frac{n_{\text{SO}_2,l}(t)}{N_l} \right) P_l}{(10^{-(\text{cloud pH})})^2} \right] H_4 \left(\frac{n_{\text{HCHO},l}(t)}{N_l} \right) P_l
 \end{aligned} \tag{11}$$

$$\begin{aligned}
 &+ \left(k_8 H_1 H_2 \frac{\left(\frac{n_{\text{SO}_2,l}(t)}{N_l} \right) P_l}{10^{-(\text{cloud pH})}} \right. \\
 &\quad \left. + k_9 H_1 H_2 H_3 \frac{\left(\frac{n_{\text{SO}_2,l}(t)}{N_l} \right) P_l}{(10^{-(\text{cloud pH})})^2} \right) H_4 H_7 \left(\frac{n_{\text{HCHO},l}(t)}{N_l} \right) P_l \Bigg] CLW_l \\
 L_{\text{HMS},l}(t) &= P_{\text{SO}_2,l}(t) = P_{\text{HCHO},l}(t) = k_{11} k_w \frac{\left(\frac{n_{\text{HMS},l}}{CLW_l} \right)}{10^{-(\text{cloud pH})}} CLW_l
 \end{aligned} \tag{12}$$

in which H denotes Henry's law or equilibrium constants and k represents the rate constants for the reactions 1-9. P_l is the pressure for layer l in atm, and CLW_l is the cloud liquid water content for the

layer in L m^{-3} . We find that the aqueous phase reactions under consideration are sufficiently slow (e.g., timescales greater than 10s of seconds) so as to not be limited by the mass transfer of HCHO and SO_2 from the gas into liquid phase or within the particle itself (Jacob, 2000).

S3. Comparison of cloud products, associated uncertainty, and trends

MERRA-2 provides cloud liquid water content averaged over each 0.5° by 0.625° gridbox, while CERES supplies the low cloud liquid water path (LCLWP) for just the cloudy fraction of each 1° by 1° grid box. To compare cloud liquid water in the two datasets, we multiply the LCLWP in CERES by its corresponding cloud fraction to get a grid-box averaged value; we also sum up the cloud liquid water content in MERRA-2 from the surface to 700 hPa, equal to the height used for CERES. The MERRA-2 and CERES grid boxes that include Tsinghua University (40.00°N , 116.33°E) do not match in spatial extent, introducing error in the comparison. Additionally, differences in LCLWP could be caused by clouds above the boundary layer but below 700 hPa, which are outside the domain of the 1-D model.

We examine the LCLWP reported by MERRA-2 and CERES in December 2011 and January 2013, as the HMS production proposed here depends on aqueous phase reaction of HCHO and S(IV). Both MERRA-2 and CERES show the presence of low clouds during these periods, but with some differences (Figure S1). MERRA-2 cloud liquid water content, averaged across the grid box at times when clouds are present, is $4 \mu\text{L m}^{-3}$ in December 2011 and $10 \mu\text{L m}^{-3}$ in January 2013. On December 7, MERRA-2 shows a peak in LCLWP of $\sim 24 \text{ g m}^{-2}$ in contrast to a peak of only 4 g m^{-2} in CERES. Both MERRA-2 and CERES capture a peak in LCLWP on December 13, with a value of $\sim 34 \text{ g m}^{-2}$ in MERRA-2 compared to $\sim 25 \text{ g m}^{-2}$ in CERES. However, MERRA-2 appears to miss a large low cloud event on December 28-30, when CERES shows a 2-day mean of LCLWP of 17.9 g m^{-2} . In January 2013, MERRA-2 reports one-day peaks of LCLWP ranging from 33-116 g m^{-2} on the 11th, 13th and 15th, compared to 15-23 g m^{-2} in CERES. For our model simulation, we apply the MERRA-2 cloud liquid water content in the boundary layer, which comprises ~ 20 -40% of LCLWP on average. This comparison with CERES, however, suggests the magnitude of the uncertainty in MERRA-2 product.

In our simulations, errors in the estimate of cloud liquid water content will affect HMS production only if these errors cause the HCHO lifetime to change relative to the lifetime of the cloud. For example, the discrepancy between MERRA-2 and CERES LCLWP on December 13, 2011, is less than an order of magnitude, implying a relatively small bias in MERRA-2 cloud liquid water content and little effect on HMS production. In contrast, the large discrepancy between MERRA-2 and CERES on

December 30 ($> 10 \text{ g m}^{-2}$) implies that HMS production could be much greater on these days. Similarly, possible biases in MERRA-2 cloud liquid water content could be significant on January 15, 2013, but not on January 11 and 13 (Figure S1).

As HMS production depends so strongly on the availability of low cloud liquid water, we examine the historical record to check for trends in low cloud cover and to determine the uniqueness of the January 2013 event. We find that mean CERES LCLWP in winter (DJF) is 4.57 g m^{-2} over 2000-2017, with a median value of 3.92 g m^{-2} . The mean for winter 2011-2012 is 5.02 g m^{-2} , while winter 2012-2013 has the highest mean low LCLWP of the entire time period, at 9.74 g m^{-2} . No long-term trend in DJF low LCLWP is revealed. Of the 54 winter months, December 2011 has the 7th mean highest value for LCLWP (7.22 g m^{-2}), while January 2013 has the 3rd highest value (11.0 g m^{-2}) after December 2012 and February 2014 (Figure S5) when high levels of particulates were also reported (Figure 3).

S4. GEOS-Chem model simulations

For our GEOS-Chem simulation we use version 11-01 (<http://acmg.seas.harvard.edu/geos/index.html>). GEOS-Chem includes a fully coupled simulation of O_3 - NO_x -VOC-aerosol chemistry (Park et al., 2004), with partitioning between the gas and aerosol phase of sulfate, nitrate, and ammonium according to the ISOROPPIA-II thermodynamic equilibrium model (Fountoukis and Nenes, 2007). We use the standard simulation which includes in-cloud aqueous phase oxidation of SO_2 by O_3 and H_2O_2 and gas-phase oxidation of SO_2 by OH (Alexander et al., 2012; Y. Wang et al., 2014). Transition metal catalyzed oxidation of SO_2 (Alexander et al., 2009) and SO_2 oxidation by NO_2 (Zhang et al., 2015) are not included in the GEOS-Chem simulations; such oxidation mechanisms are unlikely to explain the model underestimate of particulate sulfur during extreme haze events (Section S1).

Emissions used in our simulation come from the Multi-resolution Emission Inventory for China (MEIC; <http://www.meicmodel.org/>) the China component of the MIX emissions inventory for Asia (M. Li et al., 2017). MEIC contains China sector specific monthly emissions for SO_2 , NO_x , NH_3 , HCHO, BC, and OC at a $0.25 \times 0.25^\circ$ horizontal resolution. We use the nested version of GEOS-Chem with a $0.5 \times 0.625^\circ$ horizontal resolution over Asia (60° - 150°E , 11°S - 55°N) and a $2 \times 2.5^\circ$ horizontal resolution for the global simulation (Chen et al., 2009; Zhang et al., 2014). The Harvard-NASA Emissions Component in GEOS-Chem regrids all emissions fields to $0.5 \times 0.625^\circ$ horizontal resolution and adds weekly and diurnal emissions scaling factors (Keller et al., 2014).

In line with other modeling studies, GEOS-Chem simulates low levels of oxidants during winter haze events. Across December 2011 and January 2013, mean H_2O_2 in the model is ~ 0.2 ppb and mean O_3 is ~ 6 ppb. Median O_3 across these periods was only ~ 2 ppb, due to the large increases in O_3 simulated during the brief cloud- and haze-free intervals. For January 2013, when data are available, modeled O_3 is in agreement with observations of only a few ppb during haze episodes and an overall mean of 6-10 ppb (Ji et al., 2014; Quan et al., 2014; Zheng et al., 2015).

S5. Methodology followed to detect HMS using an IC system

Five sample types were prepared in order to examine the ability of ion chromatography systems to detect HMS. These included solutions of 2 and 10 mM of HMS; 2 mM of sulfate, 5 mM of HMS, and 5 mM of sulfite; 2 mM of sulfate and 2 mM of HMS; as well as 2 mM of HMS, 2 mM of sulfate, and 4 mM of sulfite. HMS and sulfate solutions were prepared by diluting formaldehyde-sodium bisulfite adduct (purity 95%, Sigma Aldrich) and sodium sulfate (purity $\geq 99\%$, Sigma Aldrich) in milli-Q water. HMS and sulfite solutions were prepared by diluting sodium bisulfite (purity $\geq 99\%$, Sigma Aldrich) in milli-Q water and performing a second dilution with the sulfite and the HMS solution. Similarly, the HMS, sulfite, and sulfate solution as well as the HMS and sulfate solution were prepared by diluting the aforementioned solutions. Each solution was examined at pH 3, 6, and 12. Hydrogen chloride was used to adjust the sample pH to 3, and sodium hydroxide was used to adjust the pH to 12. Since HMS and sulfate solutions were prepared using sodium salts, no pH adjustment was needed for samples at pH 6. We applied Ion Chromatography Dionex ICS-5000+ to examine the samples, and used two types of analytical columns: (1) the Dionex Ion Pac AS22 analytical column with the AG22 guard column and (2) the Dionex Ion Pac AS12A analytical column with the AG12A guard column. The first column setup has the same the same functional group (alkanol quaternary ammonium) and thus similar properties as the AS11 and AS11-HC columns used to make the speciated measurements of particulate sulfur, shown in Figure 2 (Wang et al., 2005; Cao et al., 2014; Cheng et al., 2016). We repeated the experiments with the second column (alkyl quaternary ammonium functional group) for comparison.

For both column setups, a carbonate/bicarbonate eluent was used in order to assure stable pH and minimal decomposition of the sample. This eluent is compatible with the AS12A and AS22 column setups. Following the extraction methods commonly used in Beijing, concentrations of particulate sulfur in $\text{PM}_{2.5}$ extracts could range from ~ 300 μM for 10 $\mu\text{g m}^{-3}$ of pure sulfate to ~ 2 mM for 70 $\mu\text{g m}^{-3}$ of pure sulfate (Wang et al., 2005). The concentrations of our samples therefore are at the

high end of what is typical for analysis of $\text{PM}_{2.5}$; however, we found minimal peak broadening for concentrations ranging from 2 μM to 4 mM, with peak half width varying between ~25 and ~40 seconds. Therefore, separation should be comparable at lower concentrations.

We find that the AS22 column cannot fully separate HMS, sulfate, and sulfite. The AS12A column, on the other hand, provides good separation between sulfate and sulfite, but cannot separate sulfite and HMS (Figure S2). In Figure S2a, the light blue line between peak 2 and peak 3 was added manually. Standard automated peak integration software for the Dionex ICS-5000+ treats both peak 2 and peak 3 as a single combined peak of sulfate. Automated quantification using sulfate calibration curves for the AS22 yields an estimate of 4.6 mM of sulfate, more than double the sulfate that was in the sample. Unless differentiated manually, the automated system therefore attributes the combined peak to sulfate, even though the peak reflects sulfate and HMS combined. Additionally, manually integrating just peak 2 still results in an estimate of more than 2 mM sulfate because some of the HMS signal contaminates peak 2.

S6. Sensitivity simulations

In this section we discuss a series of sensitivity simulations with the 1-D model carried out for January 9-17, 2013. We first examine the effect of changing cloud pH on HMS (Figure S3a). In a series of sensitivity simulations for cloud pH, we vary cloud pH from 3 to 6, based on previously discussed constraints from rainwater, aerosol and clouds. We include pH 3 to demonstrate the importance of having at least cloud pH = 4 for HMS formation. For each simulation, we apply constant emissions of HCHO and SO_2 , calculated as described in Section S1. Since the consumption rate of HCHO and SO_2 depends strongly on cloud pH, each incremental increase in pH results in greater emissions needed to maintain the specified surface concentrations of SO_2 and HCHO in step one of the emissions calculation. At cloud pH less than 4.5, peak HMS concentrations increase by as much as $\sim 30 \mu\text{g m}^{-3}$ with each incremental increase of 0.5 in cloud pH. The effect of increasing pH on peak HCHO concentrations diminishes at pH levels above 4.5. At these pH levels, however, the increase in HMS with changing cloud pH is due in large part to the increase in implied HCHO emissions. The upper limit on the supply of HCHO that reaches the cloudy layer in each of these sensitivity simulations is determined by the rate of eddy driven diffusion of HCHO from the surface. This dependence of emissions on eddy diffusion is an artifact of the model setup.

To better isolate the effect of varying cloud pH, we next conduct a series of sensitivity simulations with the same constant emissions value but with varying cloud pH. In this approach only the concentrations of H^+ and OH^- and the partitioning of sulfur species in equations 11 and 12 are changed, and the total supply of HCHO is unaffected by cloud pH or by eddy diffusion. Figure S3b shows surface HMS concentrations again under varying cloud pH conditions with constant HCHO emissions of $2.6 \times 10^{-11} \text{ kg m}^{-2} \text{ s}^{-1}$, derived from the same surface concentrations of 5.5 ppb HCHO and 50 ppb SO_2 and cloud pH of 4. Mean HMS concentration is only $0.2 \mu\text{g m}^{-3}$ at cloud pH of 3, but $13.2 \mu\text{g m}^{-3}$ at cloud pH of 6. At pH levels greater than 4.5, rapid HMS production depletes the available HCHO for the duration of the cloud, and peak concentrations of HMS saturate at $\sim 25\text{--}35 \mu\text{g m}^{-3}$. Further HMS production is limited by eddy diffusion of HCHO from the surface to the cloud layer.

Another artifact of our model set up is that the simulated HMS concentrations are sensitive to the choice of eddy diffusion coefficient. In deriving HCHO emissions, we specify the surface concentrations of HCHO. Changes in the rate of eddy diffusion affect the rate of HCHO replenishment in the cloudy layers, which in turn changes the emissions required to maintain surface HCHO concentration at constant levels. Figure S3c shows the effect of varying the eddy diffusion coefficient in the base case simulations, with cloud pH of 5 and surface concentrations of 5.5 ppb HCHO and 50 ppb SO_2 . For eddy diffusion coefficients ranging from $0.5 \times 10^5 \text{ cm}^2 \text{ s}^{-1}$ to $2 \times 10^5 \text{ cm}^2 \text{ s}^{-1}$, HCHO emissions range from $5.16 \times 10^{-11} \text{ kg m}^{-2} \text{ s}^{-1}$ to $1.16 \times 10^{-10} \text{ kg m}^{-2} \text{ s}^{-1}$, within the range of the MEIC emissions inventory (M. Li et al., 2017). Mean HMS concentrations range from $29.6 \mu\text{g m}^{-3}$ to $62.7 \mu\text{g m}^{-3}$. However, in simulations with HCHO emissions held constant, there is little effect of changing the eddy diffusion coefficient on surface HMS concentrations (Figure S3d). In these simulations, we again vary the eddy diffusion coefficient from $0.5 \times 10^5 \text{ cm}^2 \text{ s}^{-1}$ to $2 \times 10^5 \text{ cm}^2 \text{ s}^{-1}$ but set HCHO emissions at $7.70 \times 10^{-11} \text{ kg m}^{-2} \text{ s}^{-1}$, the value derived with an eddy diffusion coefficient of $1 \times 10^5 \text{ cm}^2 \text{ s}^{-1}$ and the same cloud pH and HCHO and SO_2 mean concentrations as before. Figure S3d reveals that the effect of changing the eddy diffusion coefficient on surface HMS in these simulations is minimal, with surface HMS production limited by the available HCHO.

To check that our assumption of neglecting HCHO photolysis is reasonable, we also conduct a series of simulations including HCHO loss by photolysis. We use hourly HCHO photolysis loss rates derived from the GEOS-Chem simulations described in Section S4. The hourly rates are scaled to match desired mean HCHO photolysis lifetimes that are representative of Beijing haze conditions. Photolysis is implemented in the 1-D model by adding a term to the chemical loss of HCHO (equation

11). Figure S3e shows the resulting surface HMS concentrations, with cloud pH of 5 and mean surface concentrations of 5.5 ppb HCHO and 50 ppb SO₂. In the 1-D model setup, we find that variations in the HCHO photolysis rate have minimal effect on HMS production since such variation affects only the rate of HCHO replenishment between cloud occurrences and is too slow to compete with HMS chemistry. As with the eddy diffusion coefficient, varying the photolysis rate in the 1-D model changes the emissions required to maintain surface HCHO concentration at a constant level. For HCHO lifetimes against photolysis typical of winter haze, HCHO emissions range from 9.7×10^{-11} to 1.1×10^{-10} kg m⁻² s⁻¹, within the range of the MEIC emissions inventory (M. Li et al., 2017) and similar to the emissions calculated in the base simulation.

Finally, Figure S3f shows the effect of varying the SO₂ surface concentration used to derive the implied emissions. Here again we specify cloud pH of 5 and specify mean surface concentrations HCHO of 5.5 ppb. For SO₂ concentrations spanning 5 to 75 ppb, HCHO emissions range from 4.0×10^{-11} to 8.3×10^{-11} kg m⁻² s⁻¹ and SO₂ emissions range from 8.1×10^{-11} to 7.1×10^{-10} kg m⁻² s⁻¹. Mean HMS concentrations range from 18.4 to 45.4 μg m⁻³, with higher values reflecting higher specified SO₂. We find that HMS production saturates at SO₂ concentrations greater than 5 ppb, when HCHO becomes the limiting reactant.

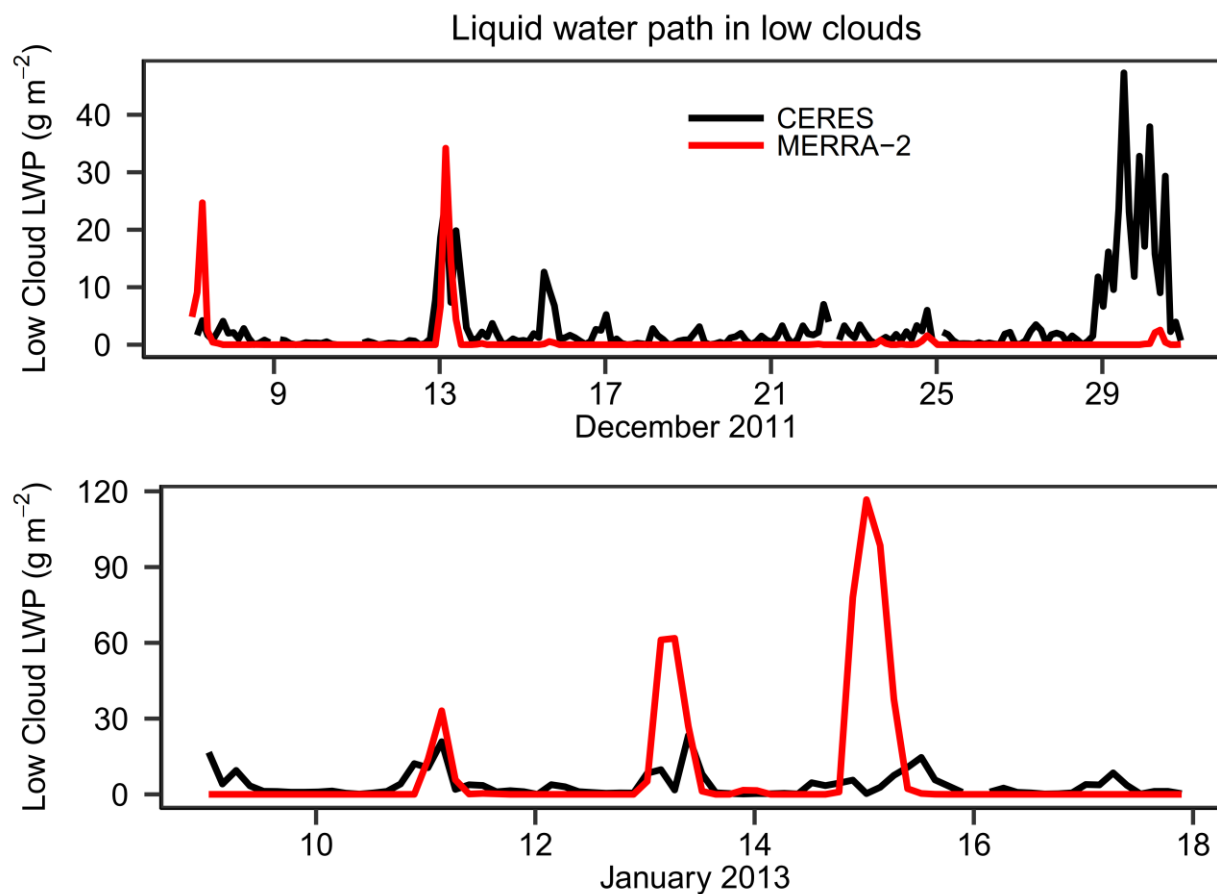


Figure S1. Timeseries of hourly liquid water path (LWP) in low clouds (> 700 hPa) in Beijing for December 2011 and January 2013. Red curves represent the assimilated LCLWP from MERRA-2; black is observed LWP from the Clouds and Earth's Radiant Energy System (CERES). For each cloud product, the values of LWP represent averages over the grid cell that includes Tsinghua University, where the measurements of sulfur particulate matter were made.

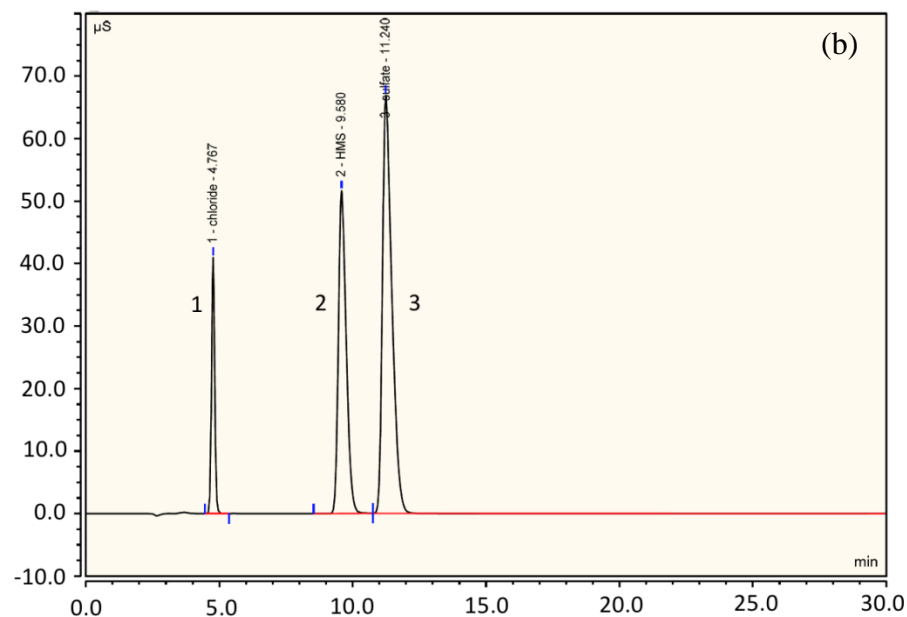
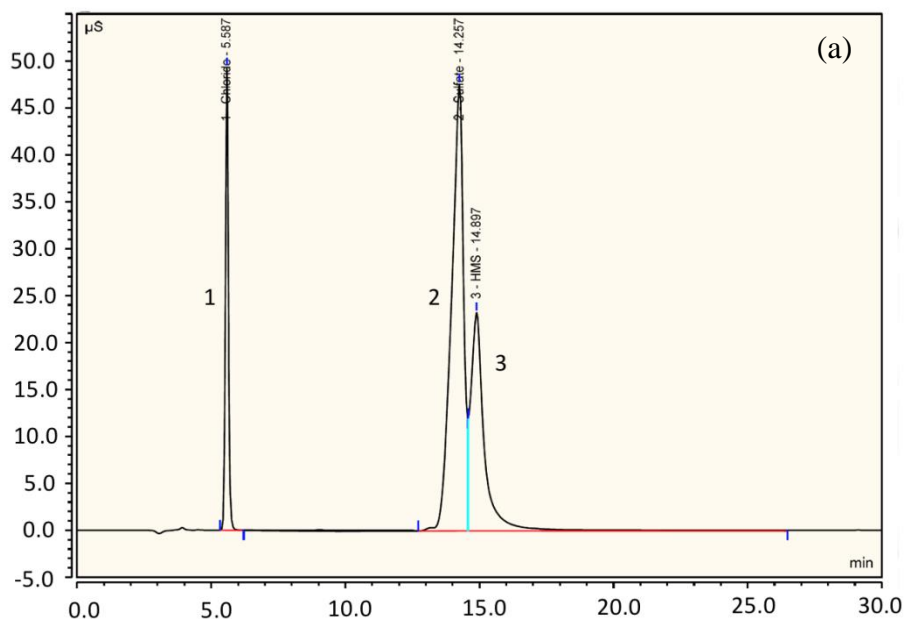


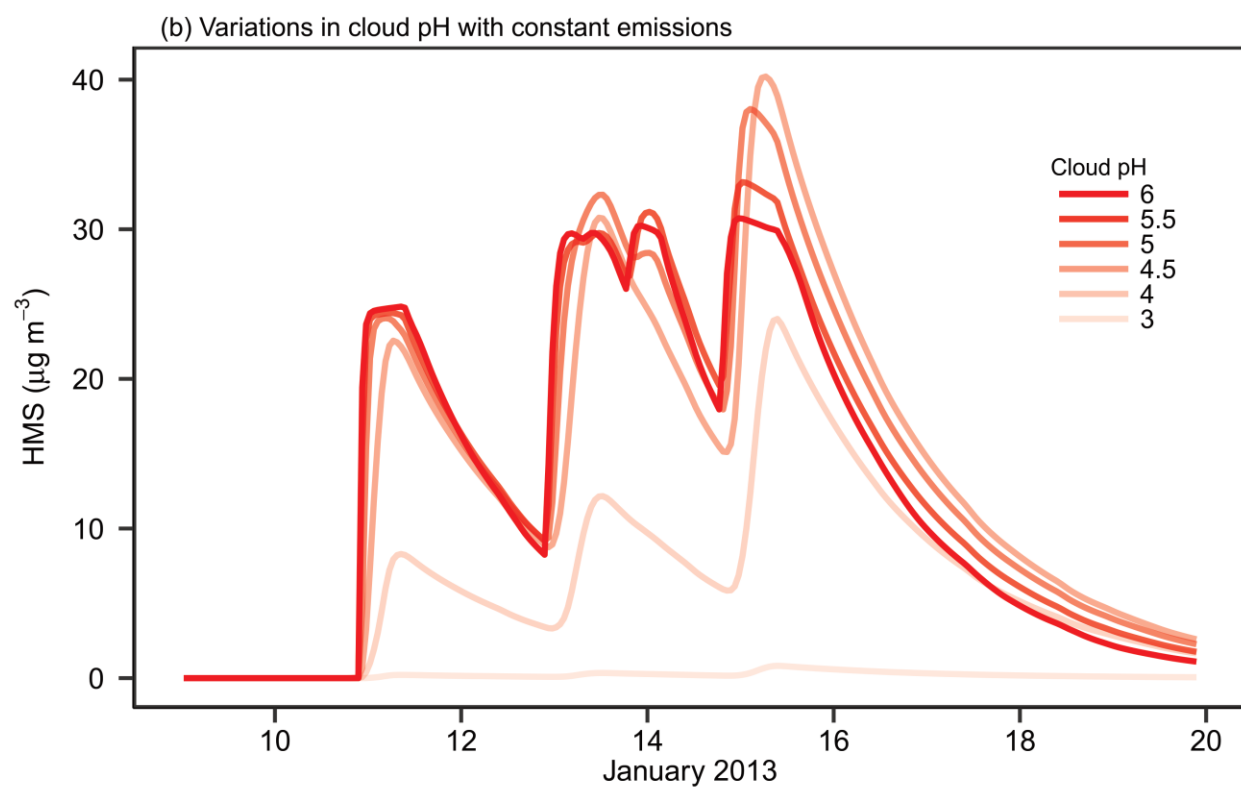
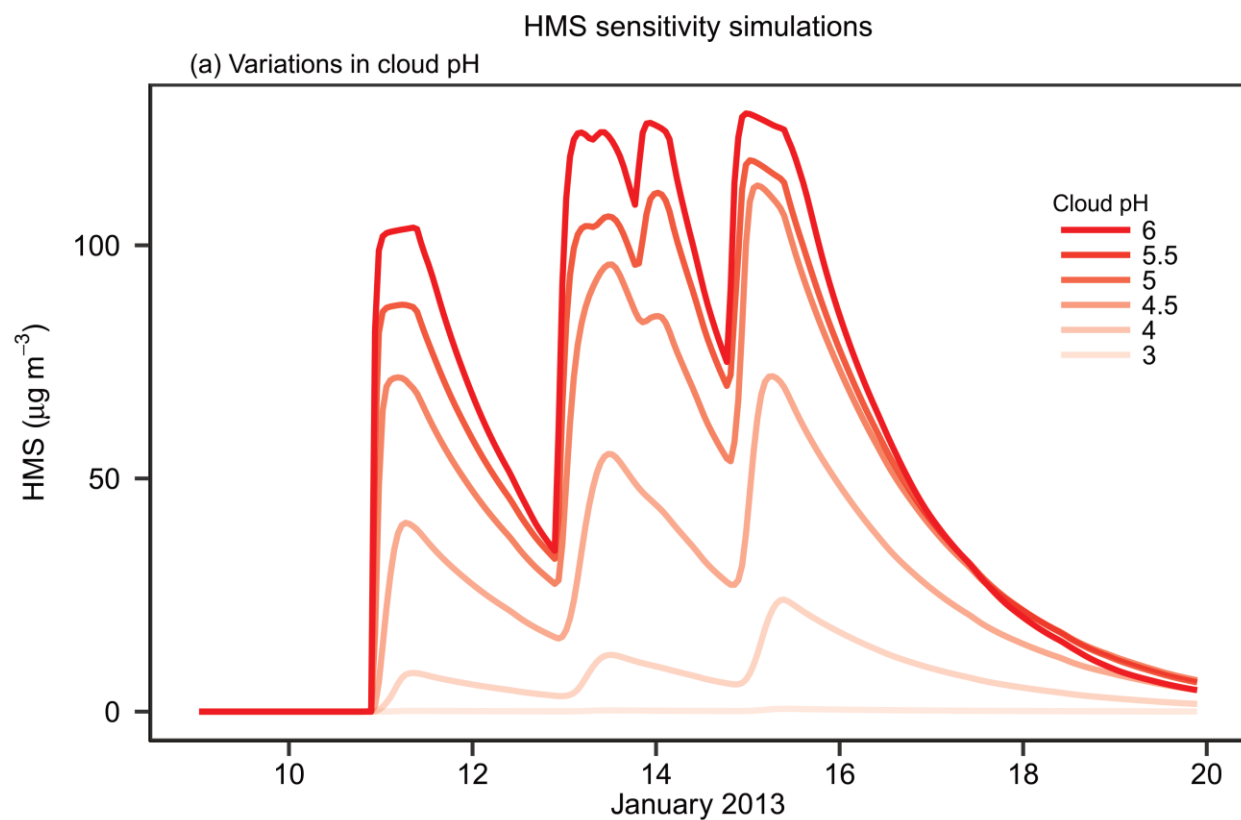
Figure S2. Example chromatographs for the detection of HMS using an Ion Chromatography system. A sample of 2 mM of HMS and 2 mM of sulfate at pH=3 was analyzed in each setup. Panel (a) shows an AS22 analytical column and AG22 guard column pair, which has similar properties as the AS11 and AS11-HC columns used for the December 2011 and January 2013 measurements. Peak 2 and peak 3, corresponding to sulfate and to HMS, are not fully separated. Standard software for automated processing of chromatographs interprets peak 2 and 3 as a combined peak corresponding to 4.6 mM

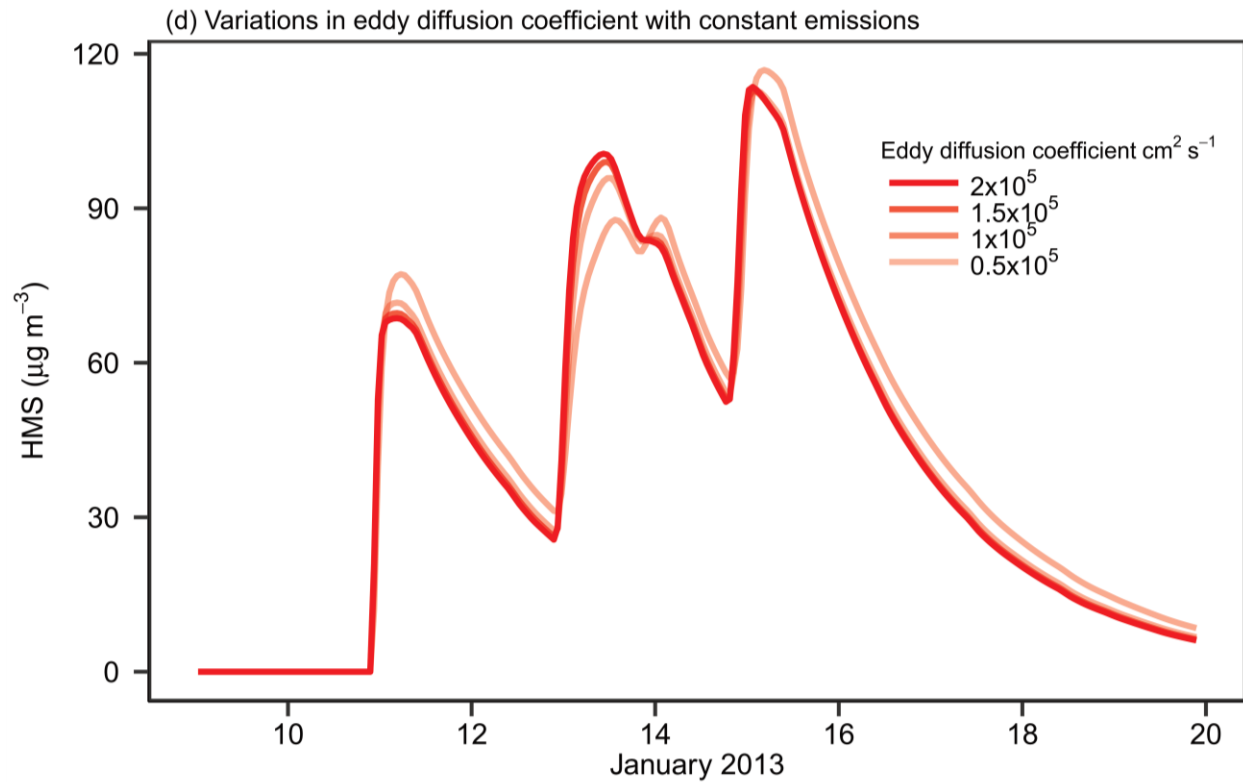
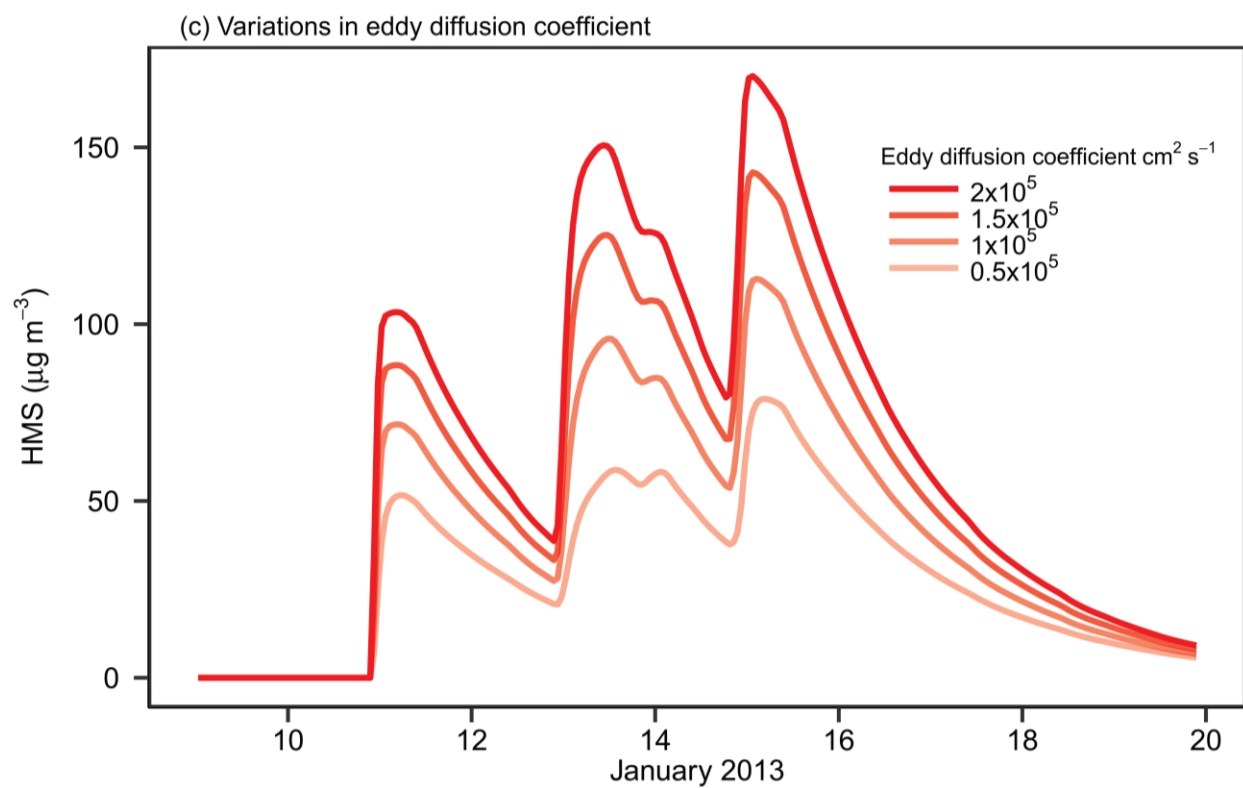
307 sulfate, roughly equivalent to the sum of 2 mM HMS and 2 mM sulfate in the sample. Panel (b) shows
308 results from an AS12A analytical column and AG12A guard column pair, which is able to successfully
309 separate HMS and sulfate.

310

311

312





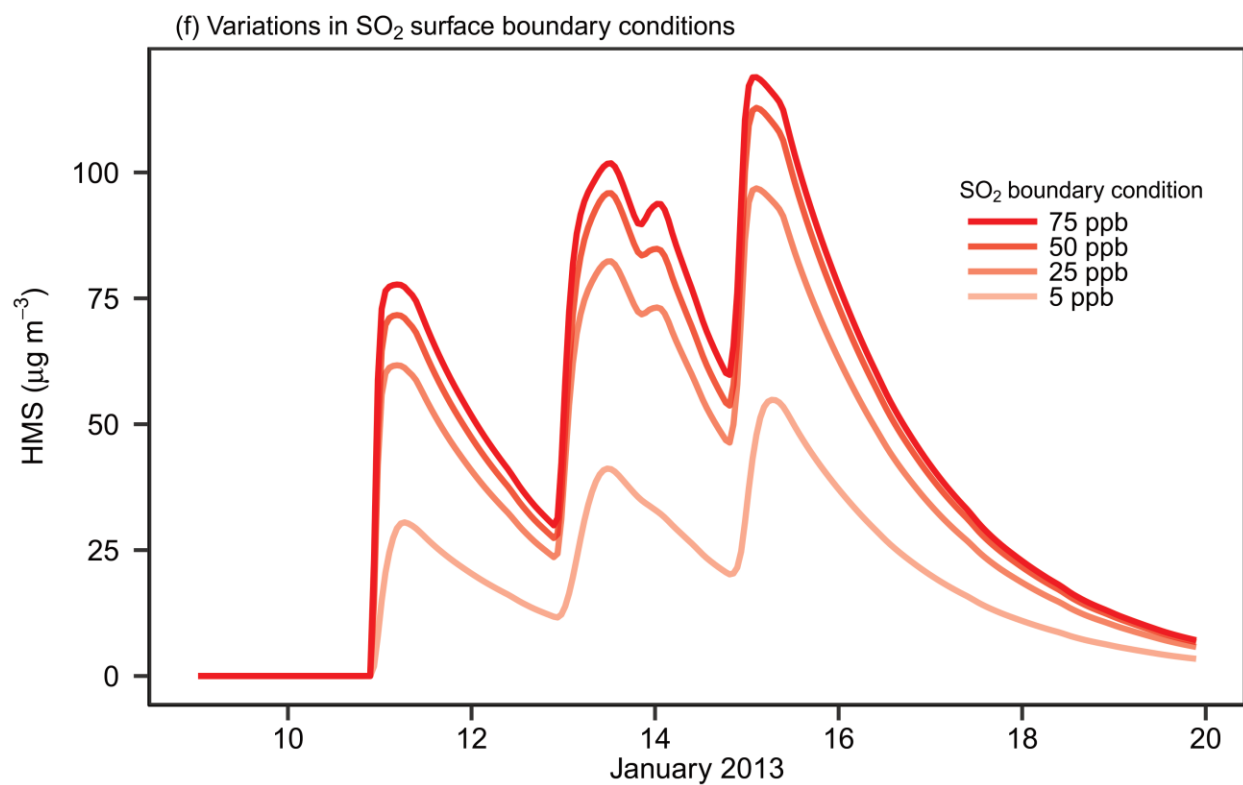
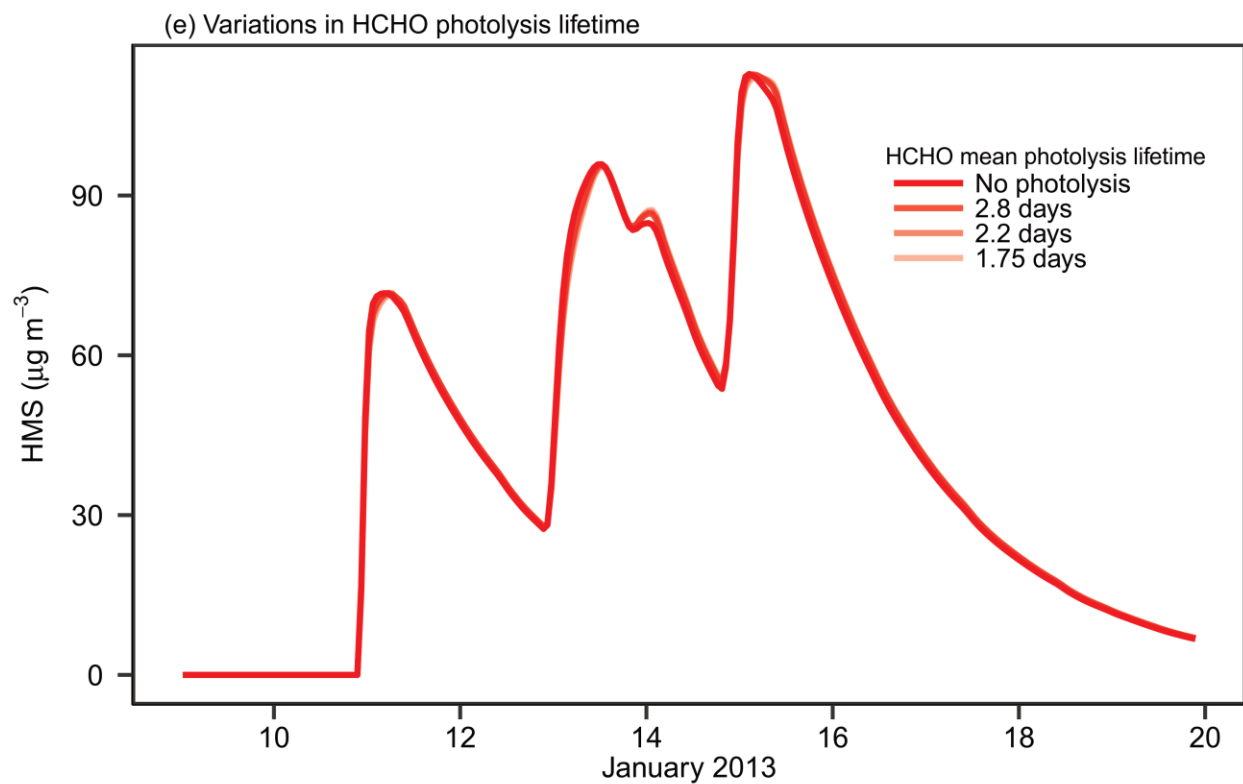


Figure S3. Timeseries of hourly HMS concentrations in Beijing in January 2013, calculated by an ensemble of sensitivity studies. Panel (a) shows the response of HMS concentrations to variations in cloud pH. Implied emissions of HCHO are allowed to vary with changing pH. The red curves in order of increasing darkness represent simulations using cloud pH from 3 to 6. Panel (b) is the same as Panel (a), but with implied emissions of HCHO fixed. Panel (c) shows the effect of varying the eddy diffusion coefficient on modeled HMS concentrations. As in panel (a), the implied emissions are permitted to vary with changing eddy diffusion. Panel (d) is the same as panel (c) but with implied emissions held constant. Panel (e) shows the effect of introducing a HCHO photolysis with timescales typical of Beijing winter haze. Panel (f) reveals the effect of varying the monthly mean SO₂ concentration used to derive the implied SO₂ emissions. The red curves in order of increasing darkness represent simulations using surface SO₂ concentrations from 5 ppb to 75 ppb SO₂.

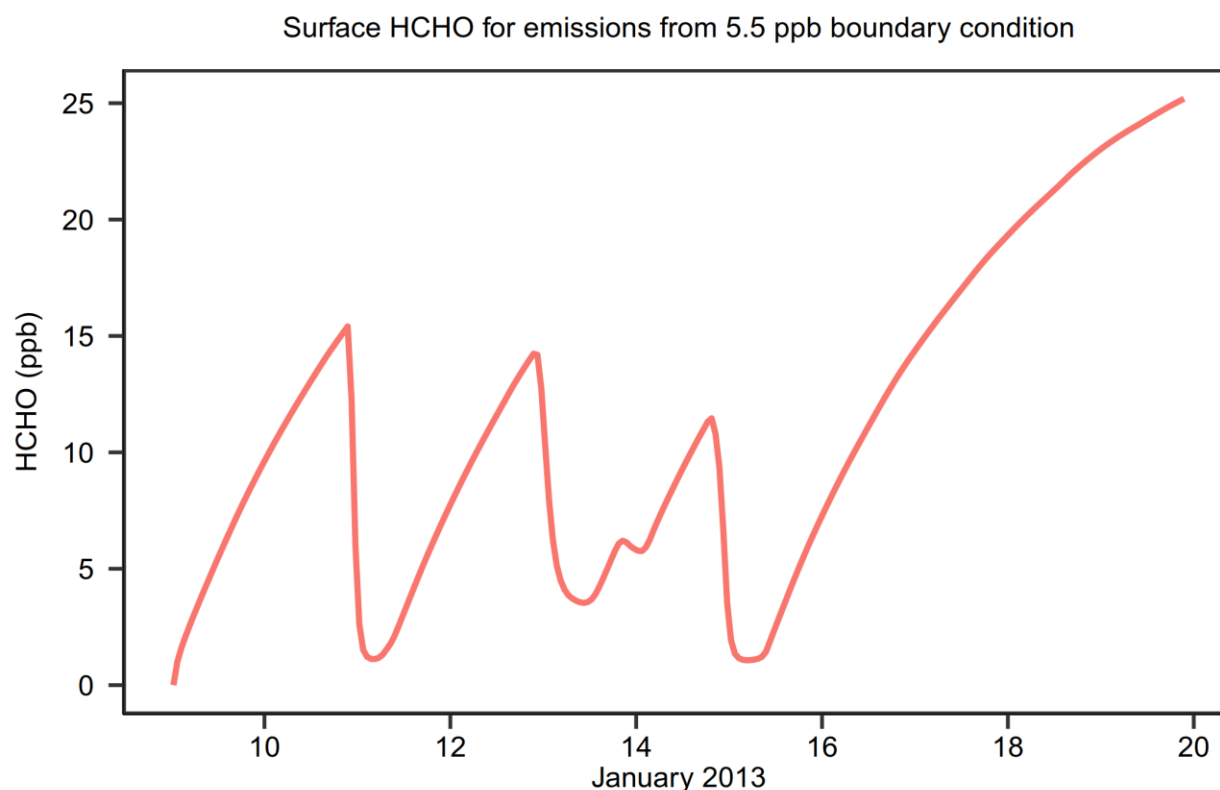


Figure S4. Simulated surface concentrations of HCHO from the 1-D model during January 2013. Shown are results for the base case, which uses constant emissions derived from a 5.5 ppb HCHO surface boundary condition. HCHO prior to January 16, the period relevant to HMS formation, ranges from 0 to ~15 ppb, similar to the variability in HCHO observed for winter 2014 in Beijing (Rao et al., 2016). After the clouds clear on January 15, HCHO climbs to high levels due to continued HCHO emissions in the absence of a chemical sink or deposition. Such high levels have not been observed, but this probable overestimate has no effect on simulated HMS in the model.

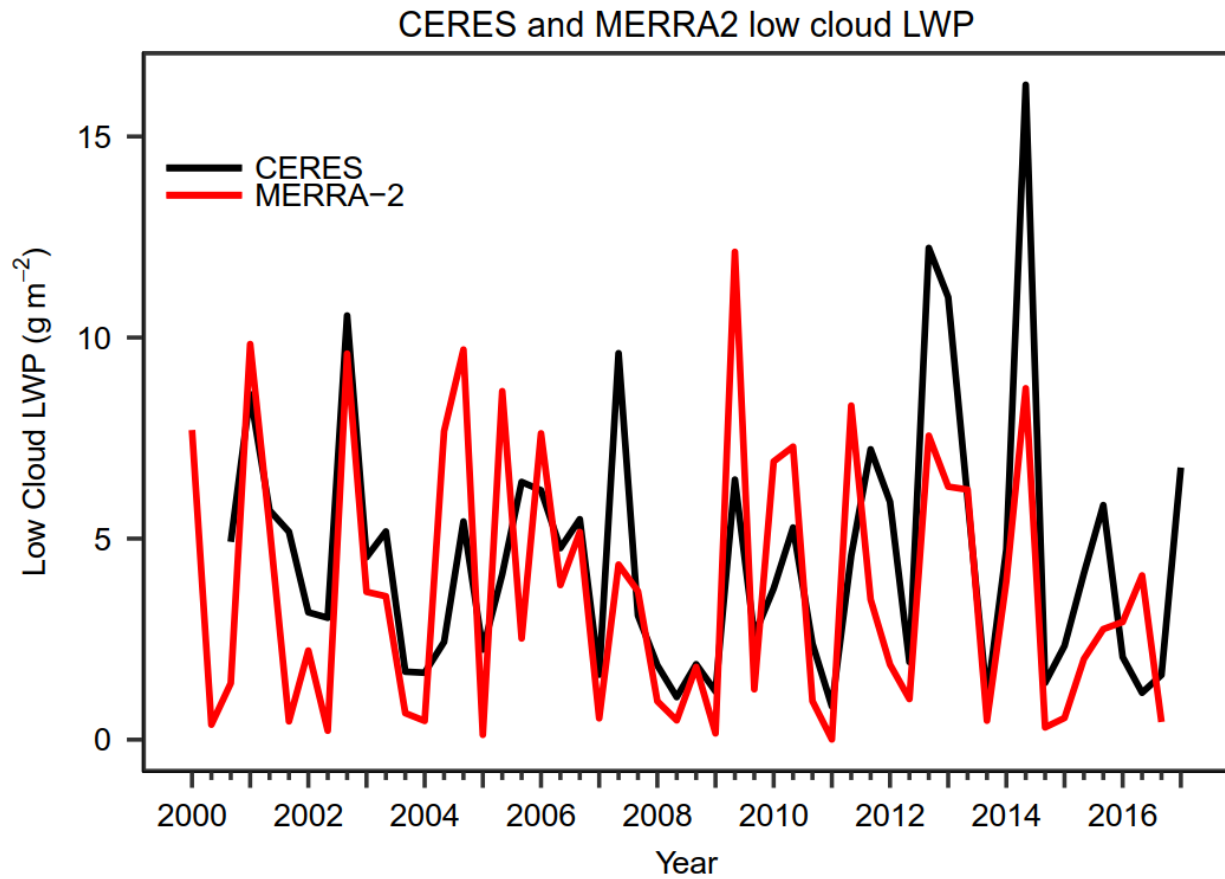


Figure S5. Timeseries of monthly mean liquid water path (LWP) in low clouds (> 700 hPa) for the winter months (December-February) from the Clouds and Earth's Radiant Energy System (CERES) and the Modern-Era Retrospective Analysis for Research and Applications, version 2 (MERRA-2) from January 2000 to January 2017. The values of LWP represent means over the CERES or MERRA-2 grid cell that includes Tsinghua University.

345 **Table S1: Constants used in 1-D model**

Abbreviation	Description	Value	Units	Reference
k_z	Eddy diffusion coefficient	1×10^5	$\text{cm}^2 \text{s}^{-1}$	Jacob et al., 1989; Roach et al., 1982
V_e	Entrainment velocity	0.5	cm s^{-1}	Jacob et al., 1989; Roach et al., 1982
$H_{1,298}$	Henry's law constant for reaction 1 at 298 K	1.214×10^{-3}	M hPa^{-1}	Munger et al., 1983
ΔH_1	Enthalpy change for reaction 1	-26.15	kJ mol^{-1}	Munger et al., 1983
$H_{2,298}$	Equilibrium constant for reaction 2 at 298 K	1.3×10^{-2}	M	Munger et al., 1983
ΔH_2	Enthalpy change for reaction 2	-17.41	kJ mol^{-1}	Munger et al., 1983
$H_{3,298}$	Equilibrium constant for reaction 3 at 298 K	6.6×10^{-8}	M	Smith and Martell, 1976; Seinfeld and Pandis, 2006
ΔH_3	Enthalpy change for reaction 3	-9.33	kJ mol^{-1}	Munger et al., 1983
$H_{4,298}$	Henry's law constant for reaction 4 at 298 K	2.5	M hPa^{-1}	Munger et al., 1983

ΔH_4	Enthalpy change for reaction 4	-53.56	kJ mol^{-1}	Munger et al., 1983
$H_{7,298}$	Equilibrium constant for reaction 7 at 298 K	2.53e3	M	Seinfeld and Pandis, 2006
ΔH_7	Enthalpy change for reaction 7	-33.39	kJ mol^{-1}	Seinfeld and Pandis, 2006
$K_{5,298}$	Rate constant at 298 K for reaction 5	7.9×10^2	$\text{M}^{-1} \text{s}^{-1}$	Boyce and Hoffman, 1984; Seinfeld and Pandis, 2006
$-E_5/R$	Activation energy for reaction 5 divided by ideal gas constant	-4900	K	Boyce and Hoffman, 1984; Seinfeld and Pandis, 2006
$K_{6f,298}$	Rate constant at 298 K for reaction 6 (forward)	2.5×10^7	$\text{M}^{-1} \text{s}^{-1}$	Boyce and Hoffman, 1984; Seinfeld and Pandis, 2006
$-E_{6f}/R$	Activation energy for reaction 6 (forward) divided by ideal gas constant	-1800	K	Boyce and Hoffman, 1984; Seinfeld and Pandis, 2006
$K_{6r,298}$	Rate constant at 298 K for 6 (reverse)	8.5×10^3	$\text{M}^{-1} \text{s}^{-1}$	Deister et al., 1986

$-E_{6r}/R$	Activation energy for reaction 6 (reverse) divided by ideal gas constant	-4500	K	Munger et al., 1986; Seinfeld and Pandis, 2006
$K_{8,298}$	Rate constant at 298 K for reaction 8	0.48	$M^{-1} s^{-1}$	Kovacs et al., 2006
$-E_8/R$	Activation energy for reaction 8 divided by ideal gas constant	-4900	K	Boyce and Hoffman, 1984; Seinfeld and Pandis, 2006
$K_{9,298}$	Rate constant at 298 K for reaction 9	2.5	$M^{-1} s^{-1}$	Kovacs et al., 2006
$-E_9/R$	Activation energy for reaction 9 divided by ideal gas constant	-1800	K	Boyce and Hoffman, 1984; Seinfeld and Pandis, 2006
$K_{w,298}$	Equilibrium constant for water self-ionization at 298 K	1×10^{-14}	M^2	Smith and Martell, 1976; Seinfeld and Pandis, 2006
ΔH_w	Enthalpy change for water self-ionization	-55.86	Kcal mol ⁻¹	Smith and Martell, 1976; Seinfeld and Pandis, 2006

346

347

348

349

References

- Alexander, B., Allman, D. J., Amos, H. M., Fairlie, T. D., Dachs, J., Hegg, D. A., & Sletten, R. S. (2012). Isotopic constraints on the formation pathways of sulfate aerosol in the marine boundary layer of the subtropical northeast Atlantic Ocean. *Journal of Geophysical Research: Atmospheres*, 117(D6), D06304. <https://doi.org/10.1029/2011JD016773>
- Alexander, Becky, Park, R. J., Jacob, D. J., & Gong, S. (2009). Transition metal-catalyzed oxidation of atmospheric sulfur: Global implications for the sulfur budget. *Journal of Geophysical Research: Atmospheres*, 114(D2), D02309. <https://doi.org/10.1029/2008JD010486>
- Boyce, S. D., & Hoffmann, M. R. (1984). Kinetics and mechanism of the formation of hydroxymethanesulfonic acid at low pH. *The Journal of Physical Chemistry*, 88(20), 4740–4746.
- Cao, C., Jiang, W., Wang, B., Fang, J., Lang, J., Tian, G., et al. (2014). Inhalable Microorganisms in Beijing's PM_{2.5} and PM₁₀ Pollutants during a Severe Smog Event. *Environmental Science & Technology*, 48(3), 1499–1507. <https://doi.org/10.1021/es4048472>
- Chen, D., Wang, Y., McElroy, M. B., He, K., Yantosca, R. M., & Le Sager, P. (2009). Regional CO pollution and export in China simulated by the high-resolution nested-grid GEOS-Chem model. *Atmos. Chem. Phys.*, 9(11), 3825–3839. <https://doi.org/10.5194/acp-9-3825-2009>
- Cheng, Yafang, Zheng, G., Wei, C., Mu, Q., Zheng, B., Wang, Z., et al. (2016). Reactive nitrogen chemistry in aerosol water as a source of sulfate during haze events in China. *Science Advances*, 2(12), e1601530. <https://doi.org/10.1126/sciadv.1601530>
- Cheng, Yuan, He, K., Du, Z., Engling, G., Liu, J., Ma, Y., et al. (2016). The characteristics of brown carbon aerosol during winter in Beijing. *Atmospheric Environment*, 127, 355–364. <https://doi.org/10.1016/j.atmosenv.2015.12.035>
- Deister, U., Neeb, R., Helas, G., & Warneck, P. (1986). Temperature dependence of the equilibrium $\text{CH}_2(\text{OH})_2 + \text{HSO}_3^- = \text{CH}_2(\text{OH})\text{SO}_3^- + \text{H}_2\text{O}$ in aqueous solution. *The Journal of Physical Chemistry*, 90(14), 3213–3217. <https://doi.org/10.1021/j100405a033>
- Fairlie, T. D., Jacob, D. J., Dibb, J. E., Alexander, B., Avery, M. A., van Donkelaar, A., & Zhang, L. (2010). Impact of mineral dust on nitrate, sulfate, and ozone in transpacific Asian pollution plumes. *Atmos. Chem. Phys.*, 10(8), 3999–4012. <https://doi.org/10.5194/acp-10-3999-2010>
- Fountoukis, C., & Nenes, A. (2007). ISORROPIA II: a computationally efficient thermodynamic equilibrium model for $\text{K}^+ - \text{Ca}^{2+} - \text{Mg}^{2+} - \text{NH}_4^+ - \text{Na}^+ - \text{SO}_4^{2-} - \text{NO}_3^- - \text{Cl}^- - \text{H}_2\text{O}$ aerosols. *Atmos. Chem. Phys.*, 7(17), 4639–4659. <https://doi.org/10.5194/acp-7-4639-2007>

381 Gelaro, R., McCarty, W., Suárez, M. J., Todling, R., Molod, A., Takacs, L., et al. (2017). The Modern-Era
 382 Retrospective Analysis for Research and Applications, Version 2 (MERRA-2). *Journal of Climate*,
 383 30(14), 5419–5454. <https://doi.org/10.1175/JCLI-D-16-0758.1>
 384 Guo, H., Weber, R. J., & Nenes, A. (2017). High levels of ammonia do not raise fine particle pH
 385 sufficiently to yield nitrogen oxide-dominated sulfate production. *Scientific Reports*, 7(1), 12109.
 386 <https://doi.org/10.1038/s41598-017-11704-0>
 387 Harris, E., Sinha, B., Pinxteren, D. van, Tilgner, A., Fomba, K. W., Schneider, J., et al. (2013). Enhanced Role
 388 of Transition Metal Ion Catalysis During In-Cloud Oxidation of SO₂. *Science*, 340(6133), 727–730.
 389 <https://doi.org/10.1126/science.1230911>
 390 Jacob, D. J. (1986). Chemistry of OH in remote clouds and its role in the production of formic acid and
 391 peroxymonosulfate. *Journal of Geophysical Research: Atmospheres*, 91(D9), 9807–9826.
 392 <https://doi.org/10.1029/JD091iD09p09807>
 393 Jacob, D. J., Gottlieb, E. W., & Prather, M. J. (1989). Chemistry of a polluted cloudy boundary layer.
 394 *Journal of Geophysical Research: Atmospheres*, 94(D10), 12975–13002.
 395 <https://doi.org/10.1029/JD094iD10p12975>
 396 Jacob, D. J. (2000). Heterogeneous chemistry and tropospheric ozone. *Atmospheric Environment*,
 397 34(12), 2131–2159. [https://doi.org/10.1016/S1352-2310\(99\)00462-8](https://doi.org/10.1016/S1352-2310(99)00462-8)
 398 Ji, D., Li, L., Wang, Y., Zhang, J., Cheng, M., Sun, Y., et al. (2014). The heaviest particulate air-pollution
 399 episodes occurred in northern China in January, 2013: Insights gained from observation.
 400 *Atmospheric Environment*, 92, 546–556. <https://doi.org/10.1016/j.atmosenv.2014.04.048>
 401 Keller, C. A., Long, M. S., Yantosca, R. M., Da Silva, A. M., Pawson, S., & Jacob, D. J. (2014). HEMCO v1.0: a
 402 versatile, ESMF-compliant component for calculating emissions in atmospheric models. *Geosci.*
 403 *Model Dev.*, 7(4), 1409–1417. <https://doi.org/10.5194/gmd-7-1409-2014>
 404 Kovacs, K., McIlwaine, R., Gannon, K., Taylor, A. F., & Scott, S. K. (2005). Complex Behavior in the
 405 Formaldehyde–Sulfite Reaction. *The Journal of Physical Chemistry A*, 109(1), 283–288.
 406 <https://doi.org/10.1021/jp0464324>
 407 Li, M., Zhang, Q., Kurokawa, J.-I., Woo, J.-H., He, K., Lu, Z., et al. (2017). MIX: a mosaic Asian
 408 anthropogenic emission inventory under the international collaboration framework of the MICS-
 409 Asia and HTAP. *Atmos. Chem. Phys.*, 17(2), 935–963. <https://doi.org/10.5194/acp-17-935-2017>
 410 Liu, J., Zhu, L., Wang, H., Yang, Y., Liu, J., Qiu, D., et al. (2016). Dry deposition of particulate matter at an
 411 urban forest, wetland and lake surface in Beijing. *Atmospheric Environment*, 125, 178–187.
 412 <https://doi.org/10.1016/j.atmosenv.2015.11.023>

413 Liu, M., Song, Y., Zhou, T., Xu, Z., Yan, C., Zheng, M., et al. (2017). Fine particle pH during severe haze
 414 episodes in northern China. *Geophysical Research Letters*, 2017GL073210.
 415 <https://doi.org/10.1002/2017GL073210>
 416 Minnis, P., Sun-Mack, S., Young, D. F., Heck, P. W., Garber, D. P., Chen, Y., et al. (2011). CERES Edition-2
 417 Cloud Property Retrievals Using TRMM VIRS and Terra and Aqua MODIS Data – Part I: Algorithms.
 418 *IEEE Transactions on Geoscience and Remote Sensing*, 49(11), 4374–4400.
 419 <https://doi.org/10.1109/TGRS.2011.2144601>
 420 Munger, J. William, Jacob, D. J., Waldman, J. M., & Hoffmann, M. R. (1983). Fogwater chemistry in an
 421 urban atmosphere. *Journal of Geophysical Research: Oceans*, 88(C9), 5109–5121.
 422 <https://doi.org/10.1029/JC088iC09p05109>
 423 Olson, T. M., & Hoffmann, M. R. (1986). On the kinetics of formaldehyde-S(IV) adduct formation in
 424 slightly acidic solution. *Atmospheric Environment* (1967), 20(11), 2277–2278.
 425 [https://doi.org/10.1016/0004-6981\(86\)90318-5](https://doi.org/10.1016/0004-6981(86)90318-5)
 426 Park, R. J., Jacob, D. J., Field, B. D., Yantosca, R. M., & Chin, M. (2004). Natural and transboundary
 427 pollution influences on sulfate-nitrate-ammonium aerosols in the United States: Implications for
 428 policy. *Journal of Geophysical Research: Atmospheres*, 109(D15), D15204.
 429 <https://doi.org/10.1029/2003JD004473>
 430 Quan, J., Tie, X., Zhang, Q., Liu, Q., Li, X., Gao, Y., & Zhao, D. (2014). Characteristics of heavy aerosol
 431 pollution during the 2012–2013 winter in Beijing, China. *Atmospheric Environment*, 88, 83–89.
 432 <https://doi.org/10.1016/j.atmosenv.2014.01.058>
 433 Rao, Z., Chen, Z., Liang, H., Huang, L., & Huang, D. (2016). Carbonyl compounds over urban Beijing:
 434 Concentrations on haze and non-haze days and effects on radical chemistry. *Atmospheric*
 435 *Environment*, 124, Part B, 207–216. <https://doi.org/10.1016/j.atmosenv.2015.06.050>
 436 Roach, W. T., Brown, R., Caughey, S. J., Crease, B. A., & Slingo, A. (1982). A field study of nocturnal
 437 stratocumulus: I. Mean structure and budgets. *Quarterly Journal of the Royal Meteorological*
 438 *Society*, 108(455), 103–123. <https://doi.org/10.1002/qj.49710845507>
 439 Seinfeld, J. H., & Pandis, S. N. (2006). *Atmospheric Chemistry and Physics: From Air Pollution to Climate*
 440 *Change* (2 edition). Hoboken, N.J: Wiley-Interscience.
 441 Shampine, L., & Reichelt, M. (1997). The MATLAB ODE Suite. *SIAM Journal on Scientific Computing*, 18(1),
 442 1–22. <https://doi.org/10.1137/S1064827594276424>
 443 Smith, R. M., & Martell, A. (Eds.). (1976). *Critical Stability Constants: Inorganic Complexes* (Vol. 4). Springer
 444 US. Retrieved from <https://www.springer.com/us/book/9781475755084>

- Song, S., Gao, M., Xu, W., Shao, J., Shi, G., Wang, S., et al. (2018). Fine-particle pH for Beijing winter haze as inferred from different thermodynamic equilibrium models. *Atmos. Chem. Phys.*, 18(10), 7423–7438. <https://doi.org/10.5194/acp-18-7423-2018>
- Sun, Z., Mu, Y., Liu, Y., & Shao, L. (2013). A comparison study on airborne particles during haze days and non-haze days in Beijing. *Science of The Total Environment*, 456–457, 1–8. <https://doi.org/10.1016/j.scitotenv.2013.03.006>
- Wang, G., Zhang, R., Gomez, M. E., Yang, L., Zamora, M. L., Hu, M., et al. (2016). Persistent sulfate formation from London Fog to Chinese haze. *Proceedings of the National Academy of Sciences*, 113(48), 13630–13635. <https://doi.org/10.1073/pnas.1616540113>
- Wang, X., Wang, W., Yang, L., Gao, X., Nie, W., Yu, Y., et al. (2012). The secondary formation of inorganic aerosols in the droplet mode through heterogeneous aqueous reactions under haze conditions. *Atmospheric Environment*, 63, 68–76.
- Wang, Ying, Zhuang, G., Tang, A., Yuan, H., Sun, Y., Chen, S., & Zheng, A. (2005). The ion chemistry and the source of PM_{2.5} aerosol in Beijing. *Atmospheric Environment*, 39(21), 3771–3784. <https://doi.org/10.1016/j.atmosenv.2005.03.013>
- Wang, Yuxuan, Zhang, Q., Jiang, J., Zhou, W., Wang, B., He, K., et al. (2014). Enhanced sulfate formation during China's severe winter haze episode in January 2013 missing from current models. *Journal of Geophysical Research: Atmospheres*, 119(17), 2013JD021426. <https://doi.org/10.1002/2013JD021426>
- Zhang, L., Jacob, D. J., Yue, X., Downey, N. V., Wood, D. A., & Blewitt, D. (2014). Sources contributing to background surface ozone in the US Intermountain West. *Atmos. Chem. Phys.*, 14(11), 5295–5309. <https://doi.org/10.5194/acp-14-5295-2014>
- Zhang, Lin, Liu, L., Zhao, Y., Gong, S., Zhang, X., Henze, D. K., et al. (2015). Source attribution of particulate matter pollution over North China with the adjoint method. *Environmental Research Letters*, 10(8), 084011. <https://doi.org/10.1088/1748-9326/10/8/084011>
- Zhang, Yang, & Carmichael, G. R. (1999). The Role of Mineral Aerosol in Tropospheric Chemistry in East Asia—A Model Study. *Journal of Applied Meteorology*, 38(3), 353–366. [https://doi.org/10.1175/1520-0450\(1999\)038<0353:TROMAI>2.0.CO;2](https://doi.org/10.1175/1520-0450(1999)038<0353:TROMAI>2.0.CO;2)
- Zheng, G. J., Duan, F. K., Su, H., Ma, Y. L., Cheng, Y., Zheng, B., et al. (2015). Exploring the severe winter haze in Beijing: the impact of synoptic weather, regional transport and heterogeneous reactions. *Atmos. Chem. Phys.*, 15(6), 2969–2983. <https://doi.org/10.5194/acp-15-2969-2015>